Journal of Materials Chemistry A

PAPER

View Article Online
View Journal | View Issue

Cite this: J. Mater. Chem. A, 2019, 7, 7138

Constructing metallic zinc–cobalt sulfide hierarchical core–shell nanosheet arrays derived from 2D metal–organic-frameworks for flexible asymmetric supercapacitors with ultrahigh specific capacitance and performance†

Wei Sun,[a] Yuchuan Du,[b] Guangming Wu,[a] Guohua Gao,*[a] Han Zhu,*[c] Jun Shen,[a] Kun Zhang[a] and Guozhong Cao*[d]

Received 17th December 2018
Accepted 26th February 2019

DOI: 10.1039/c8ta12153b

rsc.li/materials-a

Low capacitance and sluggish kinetics of positive and negative electrode materials are two main obstacles that restrict the electrochemical performance of flexible asymmetric supercapacitors (ASCs). In this work, an effective metal–organic framework (MOF)-derived approach is proposed to construct high-performance positive and negative electrode materials with a core–shell heterostructure. The binary MOF arrays are converted to zinc–cobalt sulfide nanosheet scaffolds with excellent conductivity and a ductile structure, which can offer an electrically and ionically conductive 3D continuous network for the growth of active materials. Based on this platform, the originally built $Ni(OH)_2$@ZnCoS-NSs are validated to be a highly capacitive positive electrode (8.1 F cm^{-2} at 3 mA cm^{-2}, *i.e.*, 2730 F g^{-1}), matching well with the similarly constructed VN@ZnCoS-NS negative electrode (1.35 F cm^{-2} at 3 mA cm^{-2}). Benefiting from the rationally engineered electrodes, the assembled ASC device can exhibit ultrahigh energy density (75 W h kg^{-1} at a power density of 0.4 kW kg^{-1}), stable electrochemical stability (82% capacitance retention even after 10 000 cycles), and excellent flexibility (92% capacitance retention after bending 4000 times). This study demonstrates an attractive strategy for the rational design of high-performance heterostructure electrodes by exploiting the compositional and structural versatility of 2D MOF arrays.

1. Introduction

With increasing demands for new-generation electronics, such as various portable electronic devices, autonomous electric vehicles, roll-up displays, *etc.*, future energy storage devices are required to be highly efficient and cost-effective, and also have both large power density and high energy density as well as good mechanical flexibility.[1–3] As one of the most promising energy storage technologies, supercapacitors (SCs) have drawn intensive attention due to their excellent performance in terms of power density, charge/discharge rates, and cycling stability.[4,5] Unfortunately, the energy density and flexibility of current SCs can hardly meet the ever-growing energy demand for various consumer electronic devices. The energy density of SCs is governed by the total specific capacitance (C) and overall cell voltage (V) of the devices according to the equation $E = 1/2CV^2$.[6] In this regard, asymmetric supercapacitors (ASCs) have been proposed as a desirable type of energy storage device because of the elevated V originating from the absolutely opposite potential window of positive and negative electrode materials. Accordingly, considerable efforts have been focused on constructing positive and negative electrode materials that can provide remarkable capacitance. Compared with carbon-based electrode materials that are based on electrostatic charge adsorption to store energy, pseudocapacitive electrode materials have been widely employed as positive and negative electrode materials in ASCs because they can produce higher specific capacitance and energy density through a rapid redox reaction process.[7–9] However, these pseudocapacitive electrode materials, such as transition metal oxides (TMOs)/hydroxides and their compounds, usually have poor intrinsic conductivity and low effective utilization, which inhibit large-scale practical

[a]Shanghai Key Laboratory of Special Artificial Microstructure Materials and Technology, School of Physics Science and Engineering, Tongji University, Shanghai 200092, China. E-mail: gao@tongji.edu.cn

[b]Key Laboratory of Road and Traffic Engineering (Ministry of Education), Tongji University, Shanghai 200092, China

[c]Key Laboratory of Synthetic and Biological Colloids (Ministry of Education), School of Chemical and Material Engineering, Jiangnan University, Wuxi 214122, China. E-mail: zhuhanfj@163.com

[d]Department of Materials Science and Engineering, University of Washington Seattle, WA 98195, USA. E-mail: gzcao@uw.edu

† Electronic supplementary information (ESI) available. See DOI: 10.1039/c8ta12153b

applications.[10–12] One of the promising strategies is developing highly conductive and high load scaffolds for direct growth of the nanostructured active materials to construct core–shell heterostructures,[13–15] which indeed show outstanding electrochemical performances due to the smart hybridization of the active materials and framework in synergy.

Mixed valence oxides (MVOs), such as binary or ternary-metal oxides, have attracted enormous attention[16,17] because of their small band gap and high active sites, due to which the electronic conductivity is better than those of monometal oxides. Thus, various active materials have been widely integrated with MVOs to build core–shell heterostructures, such as MnO_2@$NiCo_2O_4$ nanosheets,[16] $Ni(OH)_2$@ZnNiCoO nanowires,[17] and $MnMoO_4$@$NiCo_2O_4$ nanocolumns.[18] Despite the fact that much progress has been achieved, further improving the performance of these implemented core–shell heterostructures, especially the specific capacitance and stability, still remains a stumbling block, probably because most of these MVOs are semiconducting, due to which the conductivity is still not sufficient for highly efficient transport of electrons. Metal sulfides commonly exhibit better electrical conductivity and higher electrochemical activity. Some of them do not have a band gap in their electronic structure and present typical metallic behavior, which can offer enhanced reaction kinetics in general under high charge/discharge rates for electrodes.[7,19,20] Compared with MVO cores, metal sulfides, especially mixed metal sulfides, are considered as an attractive secondary substrate for the growth of active materials because of their enhanced conductivity, rich redox sites, and improved structural flexibility.[2,21]

Intensive studies have demonstrated that fabrication of properly engineered core–shell arrays with well-defined morphologies and optimal conductive scaffold materials can not only enhance the conductivity and utilization of active materials, but also shorten the electron/ion diffusion path.[17,22] Metal–organic frameworks (MOFs) constructed from a wide range of metal ion and organic linkers have been considered as appealing precursors to fabricate functional materials with complex structures and controllable compositions.[23–26] Utilizing MOFs as precursors is an easily controllable and highly efficient method to fabricate target products like carbon materials (N-doped mesoporous carbon nanosheets),[27] metal oxides (hollow $NiCo_2O_4$ nanoflakes) or metal sulfides (double-shelled ZnCoS dodecahedral cages) with desired structures.[7,28] Therefore, through the delicate design and preparation of MOF precursors with tailored compositions and rational morphologies, binary metal sulfides can also be readily reconstructed from these precursors with novel structures *via* anion exchange,[29,30] and can finally lead to the construction of desirable core–shell heterostructure positive and negative electrode materials, which can entirely meet the critical requirements of high-performance ASCs.

Herein, we design and fabricate a conductive scaffold of 2D zinc–cobalt sulfide (ZnCoS) nanosheet (ZnCoS-NS) arrays on flexible carbon cloth (CC) by using Zn/Co-MOF arrays as the reactive template. Such a 2D nanosheet array network with high surface-to-bulk ratio and anisotropic structure can not only enhance the utilization of electrode materials and shorten the electron/ion diffusion path, but also easily allow the growth of other active materials. Our experimental and theoretical results (first-principles calculations) demonstrate that ZnCoS as the core exhibits excellent conductivity and a ductile structure which play a key role in fabricating high-performance electrode materials. In order to develop a high-performance ASC device, we deposit and fabricate high pseudocapacitive $Ni(OH)_2$ and VN to form 3D well-aligned $Ni(OH)_2$@ZnCoS-NS and VN@ZnCoS-NS core–shell heterostructures, which can be used as electrodes without any conductive additives or binders. Finally, the flexible ASC device with a maximum operating voltage of 1.6 V was assembled by utilizing $Ni(OH)_2$@ZnCoS-NSs as the positive electrode and VN@ZnCoS-NSs as the negative electrode with KOH poly(vinyl alcohol) (PVA) as the gel electrolyte. This device can deliver high energy density (75 W h kg^{-1}) and excellent specific capacitance (210.7 F g^{-1}) and outperforms nearly all previous flexible asymmetric supercapacitor devices.

2. Experimental section

2.1. Synthesis of Zn/Co-MOF nanosheets/CC

The synthesis procedure followed that in previous work with modifications.[31] 1 mmol $Zn(NO_3)_2 \cdot 6H_2O$ and 2 mmol $Co(NO_3)_2 \cdot 6H_2O$ were dissolved in 50 mL of DI water. 16 mmol 2-MIM was dissolved in another 50 mL of DI water. And then the former salt solution was poured into the latter ligand solution under vigorous stirring at room temperature. After 60 s, stirring was stopped, and a piece of the above-mentioned CC substrate ($3 \times 5 \times 0.025$ cm^3) was immersed into the mixture and kept at room temperature for 3 h. Later, the CC substrate, which became purple, was taken out and washed with water and vacuum dried overnight. The loading of MOFs is about 2.5 mg cm^{-2}.

2.2. Synthesis of arrays of ZnCoS-NSs/CC

The Zn/Co MOFs-NSs/CC was first annealed at 500 °C under a N_2 flow of 100 mL min^{-1} for 1 h in a tube furnace. The temperature was then dropped to 350 °C, after which the samples were further annealed in air at 350 °C for 2 h. To fabricate ZnCoS-NSs, the as-annealed sample was sulfurized *via* a hydrothermal anion-exchange reaction.[22,29] The as-prepared sample was immersed in 25 mL of a 0.1 M Na_2S solution and transferred into a Teflon-lined stainless steel autoclave. The autoclave was sealed and maintained at 95 °C for 18 h. After cooling down to room temperature, the resulting product was washed repeatedly with DI water and vacuum dried overnight.

2.3. Synthesis of $Ni(OH)_2$@ZnCoS-NSs/CC and VN@ZnCoS-NSs/CC

The above ZnCoS-NSs were used as the scaffold for $Ni(OH)_2$ nanosheet shell growth *via* a facile cathodic electrodeposition method in a 0.1 M $Ni(NO_3)_2 \cdot 6H_2O$ electrolyte solution at an electrodeposition potential of −1.0 V for 500 s. In a three-electrode system, the as-fabricated ZnCoS-NS/CC substrate, a platinum plate, and a saturated calomel electrode were used as the working, counter, and reference electrodes, respectively. The

obtained product was washed with deionized and ethanol several times, and finally dried at 60 °C in a vacuum overnight. VN was directly grown on the ZnCoS-NSs by a simple solvothermal method followed by thermal treatment in an NH_3 atmosphere. Briefly, 0.1 mL of vanadium oxytriisopropoxide (VOT) was added to 25 mL of isopropanol (IPA) with stirring at room temperature. After 30 min, the as-fabricated ZnCoS-NS/CC substrate and the solution were transferred into a Teflon-lined stainless steel autoclave, which was sealed and maintained at 200 °C for 12 h. Afterward, the substrate was taken out and washed in ethanol, and dried at 60 °C overnight under vacuum. Finally, the as-fabricated product was converted into VN@ZnCoS-NSs/CC by directly annealing under a 50 sccm NH_3 and 100 sccm Ar gas flow at 500 °C for 2 h at a heating rate of 5 °C min^{-1}. For comparison, the unitary VN nanosheets were directly grown on the CC substrate using the same procedure.

2.4. Materials characterization

The samples were characterized using SEM (XL30FEG), TEM (JEOL JEM-2100), XRD (Rigaku D/max-C with a Cu Kα radiation source), and Raman spectroscopy (Jobin-Yvon HR800, the incident wavelength is 514 nm). XPS measurements were performed using a PHI 5300 spectrometer (Perkin-Elmer) operated at 14 kV.

2.5. Electrochemical measurements

The electrochemical performance of the individual electrodes was investigated using a three-electrode measuring system in a 2 M KOH aqueous solution. $Ni(OH)_2$@ZnCoS-NSs/CC and VN@ZnCoS-NSs/CC were directly used as the working electrode. A Pt plate and a saturated calomel electrode (SCE) were selected as the counter electrode and the reference electrode, respectively. The flexible ASC device was assembled by first immersing the as-fabricated positive and negative electrodes into the KOH/PVA gel electrolyte and then keeping them under ambient conditions for 1 min. Finally, they were integrated face-to-face. Noticeably, charge balance theory was used to decide the mass loading of the positive and negative electrodes, which was about 1.1 and 1.8 mg cm^{-2}, respectively. The electrochemical electrode measurements including CV, GCD, and EIS were performed on an electrochemical workstation (CHI 660E, Shanghai Chenhua Instrument Co., Shanghai, China).

3. Results and discussion

The fabrication process for the $Ni(OH)_2$@ZnCoS-NS positive electrode and VN@ZnCoS-NS negative electrode on carbon cloth is schematically illustrated in Fig. 1. The uniform assembly of Zn/Co-MOF nanosheet (NS) arrays is directly grown on the CC substrate with a simple solution method. The ZnCoS-NS array structure can be converted from the Zn/Co-MOF precursors subsequently by the calcination and hydrothermal anion-exchange reaction (sulfurization) process with a well-retained morphology (details in the ESI†). $Ni(OH)_2$@ZnCoS-NSs are prepared *via* a facile electrodeposition process. During electrodeposition, NO_3^- in the electrolyte can be reduced on the surface of the supporter accompanied by the generation of OH^- ions which accumulate, leading to the homogeneous precipitation of tiny $Ni(OH)_2$ nanoflakes on the ZnCoS-NS surface.[32] Finally, the hierarchical core–shell heterostructures are formed. On the other hand, the fabrication of VN@ZnCoS-NSs mainly involves two steps: a simple hydrothermal process and an annealing treatment in ammonia. First, VO_x is evenly grown on the CC by a hydrolysis reaction under hydrothermal conditions (200 °C) for 12 h. Second, to transform the as-prepared VO_x to VN without damaging the morphology coated on the nanosheets, the precursor products are further thermally annealed at 500 °C in NH_3, as described in the Experiment section.

Field-emission scanning electron microscopy (FESEM) images (Fig. 2d) reveal that Zn/Co-MOF nanosheets are

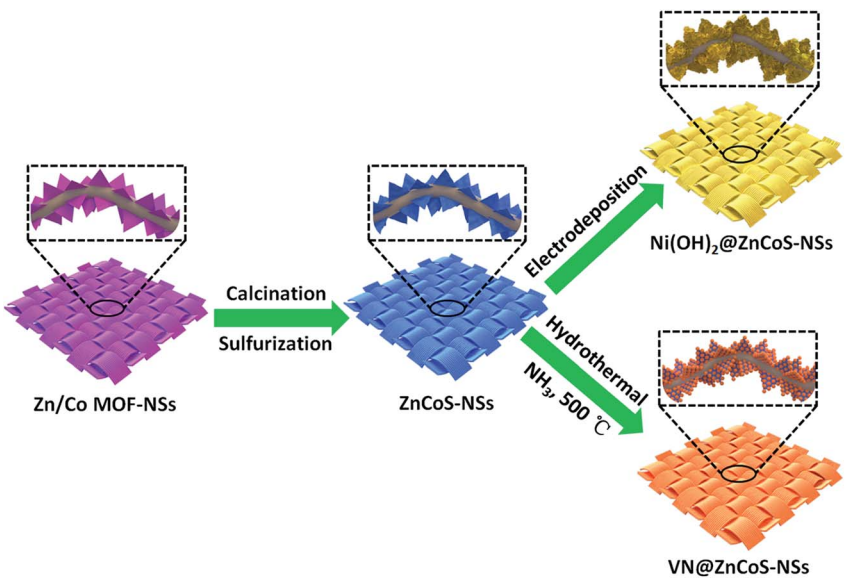

Fig. 1 Schematic illustration of the fabrication process of the $Ni(OH)_2$@ZnCoS-NS positive electrode and VN@ZnCoS-NS negative electrode.

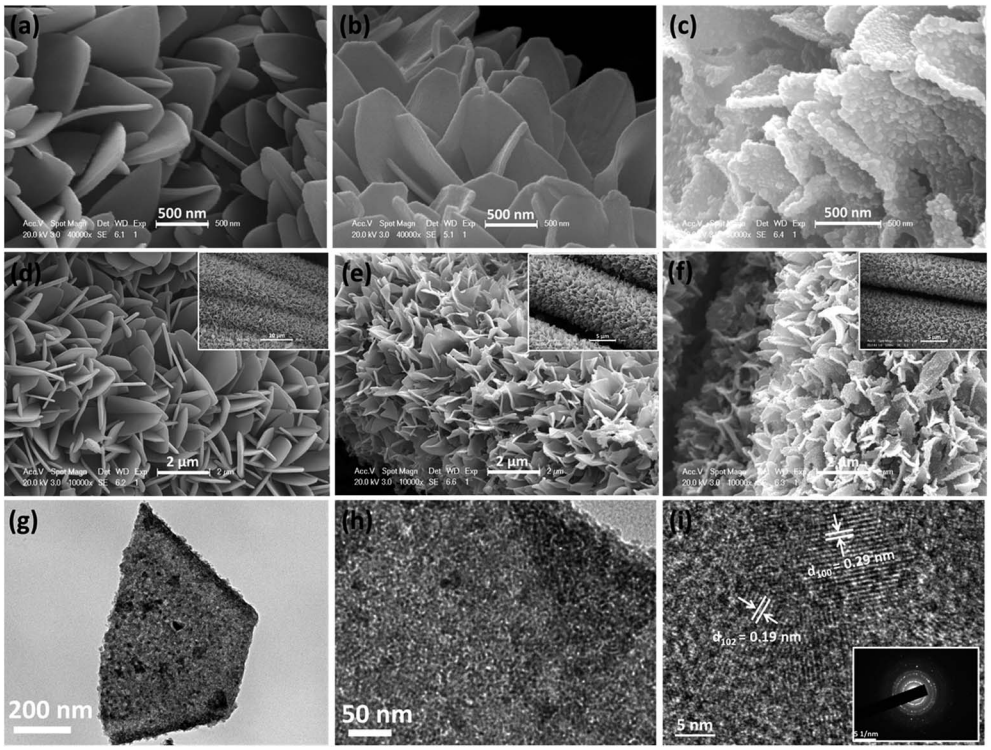

Fig. 2 SEM images of (a and d) Zn/Co-MOF nanosheets on CC, (b and e) ZnCoO-NSs/CC and (c and f) ZnCoS-NSs/CC, and TEM images (g–i) of Zn/Co MOF-derived ZnCoS-NSs with the inset in (i) showing the SAED pattern.

uniformly attached to the CC closely and have a typical 2D morphology with a thickness of around 120 nm (Fig. 2a), and a larger surface area than monometallic Co MOFs (Fig. S1a, ESI†). The crystallinity of the MOFs deposited on CC is confirmed from the X-ray diffraction (XRD) patterns depicted in Fig. S1b (ESI†), implying that the Zn/Co-based zeolitic imidazolate framework does not have any impurities.[33] After *in situ* and confined thermal treatment (Fig. 2c), it can be observed that the uniform coverage of the CC is maintained, and the overall nanosheet array structure can still be retained without agglomeration and coalescence. From the enlarged SEM image in Fig. 2b, the resultant ZnCoO-NSs become thinner and slightly titled compared with the precursor (Fig. 2a), which is mainly due to the contraction caused by decomposition of organic ligands in the MOF precursor during thermal treatment in air. In the corresponding XRD pattern (Fig. S1c, ESI†), except for the peak from the CC, all other diffraction peaks of ZnCoO-NSs can be indexed as $ZnCo_2O_4$ (JCPDS card no. 23-1390),[34,35] and the corresponding energy dispersive X-ray spectroscopy (EDS) spectrum (Fig. S1d, ESI†) reveals a Co/Zn atomic ratio of 1.92 : 1, further confirming the formation of $ZnCo_2O_4$. After exchanging with S^{2-} ions produced by Na_2S in solution, the 2D vertically aligned and interconnected structures of nanosheets are well retained and each strip of the carbon fiber is evenly covered without destroying the flexibility of the CC woven structure, as shown in Fig. 2c and f. Furthermore, the surfaces of sulfureted nanosheets (Fig. 2f) become rough due to the etching-like effect of S^{2-}.[36] Such a network architecture possesses a large surface-to-bulk ratio and the nanosheets intersect with each other, which is conducive to the growth of active materials and the formation of 3D network-like structures. Further insight into the detailed structure of ZnCoS-NSs is revealed by transmission electron microscopy (TEM) (Fig. 2g–i). The broken tips of nanosheets (Fig. 2g), caused by ultrasonication, clearly show that the ZnCoS-NSs possess a solid feature with a rough surface and a sheet-shaped structure which is consistent with the SEM analysis. A closer observation of the ZnCoS-NSs (Fig. 2h) reveals that the surface of the products possesses some pores and consists of numerous tightly interconnected nanoparticles. Meanwhile, as can be seen from the high-resolution TEM (HRTEM) image in Fig. 2i, the fringes with spacing distances of 0.29 nm and 0.19 nm match well with the (100) and (102) planes of CoS, respectively, suggesting that the as-synthesized ZnCoS-NSs are well crystallized. Furthermore, the corresponding XRD pattern is given in Fig. 3f. The diffraction peaks of ZnCoS-NSs slightly shift in comparison with the (100), (101), (102), and (110) phases of hexagonal CoS (JCPDS card no. 75-0605),[29] thus indicating the formation of Zn doped CoS, which agrees with previously reported results.[37]

The $Ni(OH)_2$@ZnCoS-NS electrode was prepared *via* a facile cathodic electrodeposition method in a 0.1 M $Ni(NO_3)_2 \cdot 6H_2O$ electrolyte solution, as expressed by the following equations:[32,38]

$$NO_3^- + 7H_2O + 8e^- \rightarrow NH_4^+ + 10OH^- \quad (1)$$

$$Ni^{2+} + 2OH^- \rightarrow Ni(OH)_2 \quad (2)$$

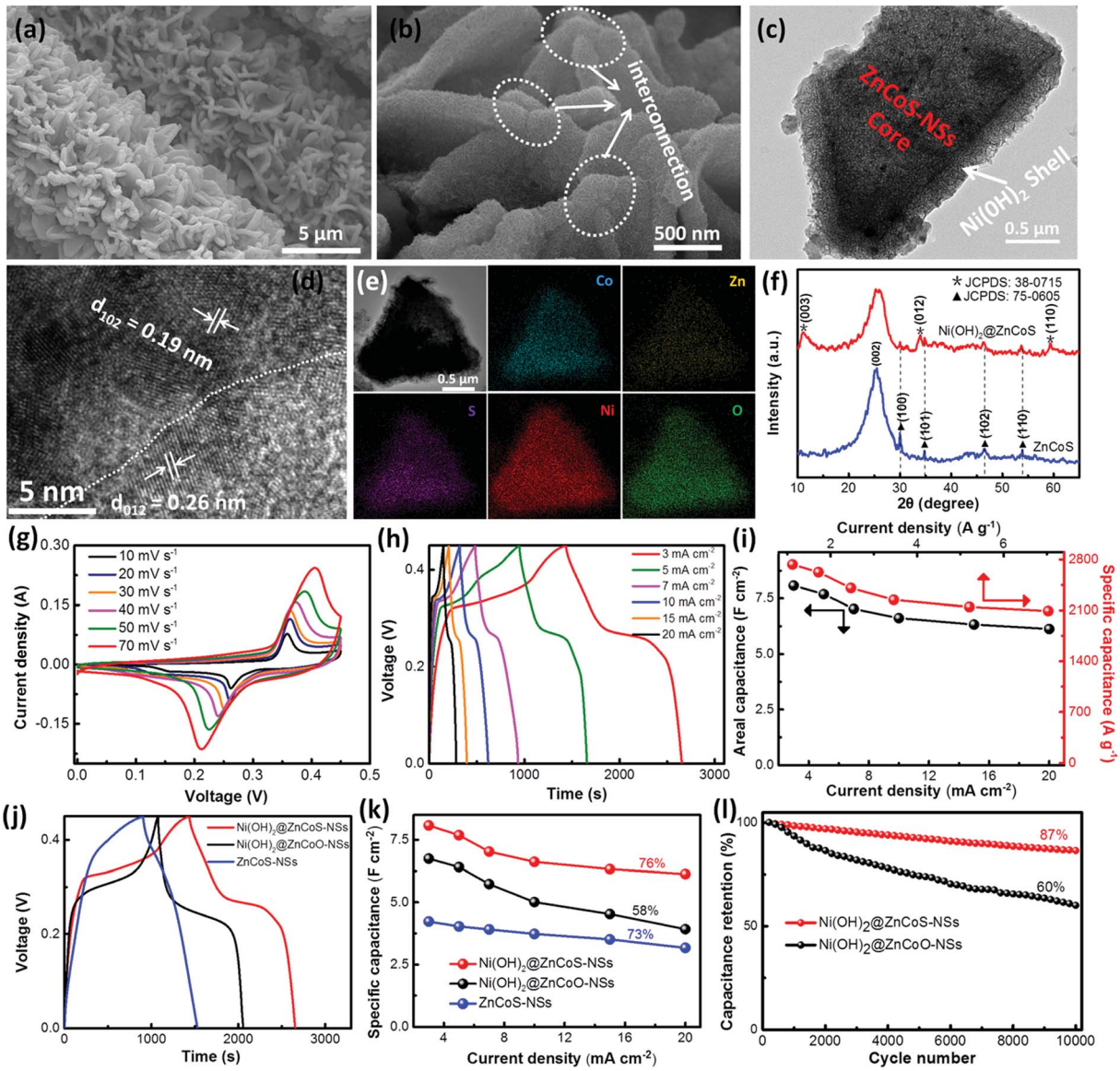

Fig. 3 Low (a) and high (b) magnification SEM images of $Ni(OH)_2$@ZnCoS-NSs; (c) typical TEM image, (d) HRTEM image, and EDS mapping results (e) of $Ni(OH)_2$@ZnCoS-NSs; (f) XRD patterns of ZnCoS-NSs and $Ni(OH)_2$@ZnCoS-NSs. Electrochemical properties of the $Ni(OH)_2$@ZnCoS-NS/CC electrode in a three-electrode system with a 2 M KOH solution: (g) CV curves at various scan rates and (h) GCD profiles at different current densities of $Ni(OH)_2$@ZnCoS-NSs; (i) areal and mass specific capacitance values *versus* current density. Comparison between the $Ni(OH)_2$@ZnCoS-NS/CC electrode, $Ni(OH)_2$@ZnCoO-NS/CC electrode, and ZnCoS-NS electrode: (j) GCD curves at a current density of 3 mA cm^{-2}, (k) areal specific capacitance values *versus* current density, and (l) cycling performance at a high current density of 20 mA cm^{-2}.

As can be clearly seen from Fig. 3a, $Ni(OH)_2$@ZnCoS-NSs still maintain highly ordered and uprightly oriented array shapes, which are well-distributed and trimly aligned along the axial direction of the carbon fibers over a large area. Clearly, at the local scale (Fig. 3b), the surfaces of ZnCoS-NSs with an average thickness of around 180 nm are homogeneously covered by dense and tiny $Ni(OH)_2$ nanoflakes as an even coating to form hierarchical core–shell heterostructures after electrodeposition, which is strikingly different from the morphology of ZnCoS-NSs (as shown in Fig. 2c). Furthermore, these as-synthesized hybrid nanosheet arrays with a lateral size of around 1 μm are in fact interconnected with each other, constructing 3D loose open nanostructures with abundant exposed surfaces and electroactive sites. One can easily see from the TEM image (Fig. 3c) that ultrathin $Ni(OH)_2$ nanoflakes are tightly and homogeneously coated on the surface of ZnCoS-NSs, consistent with the foregoing SEM result of a core–shell structure. The HRTEM image shown in Fig. 3d reveals that the heterointerface between the ZnCoS core and the $Ni(OH)_2$ shell can be clearly found and is indicated by the white line in Fig. 3d. The 0.26 and 0.19 nm lattice fringes correspond to the (012) and (102) planes of $Ni(OH)_2$ and CoS,[17,29] respectively, as evidenced by the XRD pattern (Fig. 3f). The diffraction peaks at 11.2°, 34°, and 59.6° can be indexed to the (003), (012), and (110) phases of α-$Ni(OH)_2$

(JCPDS card no. 38-0715).[17] Besides, the XRD pattern of the $Ni(OH)_2$@ZnCoS-NSs also contains the major diffraction peaks of ZnCoS without any extra peaks, indicating that the constructed core–shell heterostructures consist solely of ZnCoS and $Ni(OH)_2$. The high-angle annular dark-field scanning transmission electron microscopy (HAADF-STEM) and corresponding elemental mapping images (Fig. 3e) confirm that the Co, Zn, S, Ni, and O elements coexist and are uniformly distributed within the nanosheet framework. The signal distribution areas of the Ni and O elements are obviously larger than those of the other three elements, which provides direct evidence for the formation of a core–shell structure in the nanosheet, in which a $Ni(OH)_2$ shell coats a ZnCoS core. To further investigate the surface electronic state and chemical compositions of $Ni(OH)_2$@ZnCoS-NSs, X-ray photoelectron spectroscopy (XPS) analysis was carried out and the corresponding results are illustrated in Fig. S2 (ESI†). The XPS survey spectrum (Fig. S2a†) of the sample clearly confirms the existence of the elements Ni, O, Co, Zn, and S in $Ni(OH)_2$@ZnCoS-NSs, which is consistent with the elemental mapping results. The high-resolution spectra of Ni 2p, Co 2p, and Zn 2p (Fig. S2b–d and e†) show that the as-fabricated samples possess a mixed chemical composition containing the cations with various valence states (details in Fig. S2†), which can guarantee rich active sites and redox reactions for significantly enhancing the electrochemical performance of the electrode.[39,40] On the basis of the aforementioned analysis of the TEM, XRD, and XPS results, it can be demonstrated that the as-fabricated electrode material is composed of $Ni(OH)_2$@ZnCoS nanosheets.

The electrochemical behavior of the as-made electrode materials is investigated using a three-electrode system with a 2 M KOH aqueous solution. Fig. 3g displays the representative cyclic voltammetry (CV) curves at various scan rates from 10 to 70 mV s^{-1} and each of them shows a pair of well-defined redox peaks demonstrating typical pseudocapacitive properties. Importantly, the CV curves maintain a symmetric and similar shape at all scan rates demonstrating the ideal pseudocapacitance behavior and the rapid rate capability of the as-constructed hierarchical core–shell heterostructure. Galvanostatic charge–discharge (GCD) tests were also used to further corroborate the electrochemical behavior (Fig. 3h). With the current density increasing from 3 to 20 mA cm^{-2}, the GCD curves of $Ni(OH)_2$@ZnCoS-NSs are observed to be nonlinear and almost symmetric. However for $Ni(OH)_2$@ZnCoO-NS and ZnCoS-NS electrodes, the GCD curves (Fig. S4b and d, ESI†) exhibit a shorter discharge time and cannot remain symmetric, which suggests a low electrochemical utilization rate of the electrode materials. This result indicates that the $Ni(OH)_2$@ZnCoS-NS electrode has higher coulombic efficiency and improved pseudocapacitive properties. Furthermore, clearly different plateau regions can be observed, according to the redox peaks in CV curves. The values of specific capacitance for the $Ni(OH)_2$@ZnCoS-NS electrode (Fig. 3i) are as high as 8.1 (2730 F g^{-1}), 7.7 (2624 F g^{-1}), 7.03 (2407 F g^{-1}), 6.6 (2244 F g^{-1}), 6.33 (2147 F g^{-1}), and 6.13 (2092 F g^{-1}) F cm^{-2}, corresponding to the current densities of 3, 5, 7, 10, 15, and 20 mA cm^{-2}, respectively. Impressively, these test results significantly exceed previously reported values for Ni–Co oxides or hydroxides and mixed metal oxides/sulfides, and their corresponding heterostructure electrode materials, such as $Ni(OH)_2$@H-TiO_2 (1101.6 F g^{-1} at 1 mV s^{-1}),[41] $Ni(OH)_2$@g-C_3N_4 (1768.7 F g^{-1} at 7 A g^{-1}),[42] $Ni(OH)_2$@FeOF (1452 F g^{-1} at 1 A g^{-1}),[43] $Ni(OH)_2$@$NiCo_2O_4$/SiC (3.12 F cm^{-2} (2580 F g^{-1}) at 4.8 mA cm^{-2}),[44] and MnO_2@$CoMoO_4$ (8.01 F cm^{-2} (2666.7 F g^{-1}) at 3 mA cm^{-2}) (Table S1, ESI†).[45] Fig. 3j compares the typical GCD curves of the $Ni(OH)_2$@ZnCoS-NS, $Ni(OH)_2$@ZnCoO-NS, and ZnCoS-NS electrodes at 3 mA cm^{-2}, from which it can be seen that the as-made $Ni(OH)_2$@ZnCoS-NS electrode exhibits a substantially prolonged discharge time over $Ni(OH)_2$@ZnCoO-NSs and ZnCoS-NSs, revealing an improved capacitive behavior. Illustrated in Fig. S3 (ESI†) is a comparison of CV curves of the corresponding electrodes at a scan rate of 30 mV s^{-1}. As expected, the $Ni(OH)_2$@ZnCoS-NS electrode shows a larger CV curve area, convincingly suggesting an improved function of ZnCoS nanosheets for the growth of electrochemically active $Ni(OH)_2$. Notably, the potential separation between anodic and cathodic peaks, related to the kinetic limitation,[46] is narrowed in the CV signals of $Ni(OH)_2$@ZnCoS-NSs, as compared with those of $Ni(OH)_2$@ZnCoO-NSs, which indicates an enhanced conductance when ZnCoS is used as the scaffold. The CV and GCD curves of the $Ni(OH)_2$@ZnCoO-NS and ZnCoS-NS electrodes at different scan rates and current densities are also given in Fig. S4 (ESI†). The specific capacitance of the $Ni(OH)_2$@ZnCoS-NSs, $Ni(OH)_2$@ZnCoO-NSs and ZnCoS-NSs as a function of the current density is plotted in Fig. 3k. Obviously, the $Ni(OH)_2$@ZnCoS-NS electrode delivers a much higher capacitance of 8.1 F cm^{-2}, which is nearly 1.3 times and 2 times higher than that of the $Ni(OH)_2$@ZnCoS-NS and ZnCoS-NS electrodes at the same scan rate of 3 mA cm^{-2}, respectively. Interestingly, with the increasing scan rate up to 20 mA cm^{-2}, both $Ni(OH)_2$@ZnCoS-NSs and ZnCoS-NSs can still maintain 76% (6.2 F cm^{-2}) and 73% (3.2 F cm^{-2}) retention values, which is greatly higher than the 58% (3.92 F cm^{-2}) of $Ni(OH)_2$@ZnCoO-NSs. This clearly indicates that the improved capacitance retention arises from the contribution of the ZnCoS-NS scaffold in the heterostructure. Repeated charge/discharge tests at a high current density of 20 mA cm^{-2} are conducted to study the cycling stability of the $Ni(OH)_2$@ZnCoS-NS and $Ni(OH)_2$@ZnCoO-NS electrodes. About 87% of the initial capacitance of $Ni(OH)_2$@ZnCoS-NSs is preserved even over 10 000 cycles (Fig. 3l), which is in sharp contrast to the $Ni(OH)_2$@ZnCoO-NSs with only 60% capacitance retention. After cycling, the $Ni(OH)_2$@ZnCoS-NS electrode retains its original interconnected nanosheet morphology (Fig. S5, ESI†), implying high structural stability. These results clearly demonstrate that the key advantages of our $Ni(OH)_2$@ZnCoS-NS core–shell heterostructure are the rational structure and the tailored configuration of $Ni(OH)_2$ and the ZnCoS scaffold. Specifically, the 3D network architecture generated by the interconnected and intersecting $Ni(OH)_2$@ZnCoS nanosheets with abundant exposed surfaces can significantly maximize the accessible electroactive sites and facilitate fast ion and electron transport. Moreover, ZnCoS-NSs as the growth substrate could tremendously improve the conductivity and possess more active sites enabling a rapid reversible

faradaic reaction of $Ni(OH)_2$ nanoflakes which are then well deposited onto the ZnCoS nanosheets as the shell.

Density functional theory (DFT) calculations were used to further uncover the merits of ZnCoS as the scaffold for the growth of $Ni(OH)_2$. Based on the cubic Co_3O_4 and hexagonal CoS, optimized crystal structures of ZnCoO and ZnCoS are built and hence the density of states (DOS) calculations are performed to compare their electronic properties, which are shown in Fig. 4a–d. Fig. 4a reveals that the total DOS for ZnCoO presents the characteristics of a semiconductor, and the Fermi level (E_f) is located between the valence band (VB) and the conduction band (CB) with a band gap of 0.54 eV. Notably, from Fig. 4c, the band gap of the total DOS of ZnCoS disappeared and high density of states is observed on the E_f, which clearly demonstrates that ZnCoS exhibits obviously metallic characteristics with improved electron mobility and conductivity compared with ZnCoO, thus ensuring that the resulting heterostructure electrode exhibits higher charge-transfer kinetics and efficiency, when ZnCoS nanosheets are employed as the scaffold. To verify the above calculation results in theory, voltage drop and electrochemical impedance spectroscopy (EIS) analyses are performed. Form Fig. S6 (ESI†), the internal resistance (IR) of the $Ni(OH)_2$@ZnCoS-NS electrode is about 0.0024 V, which is much lower than that of the $Ni(OH)_2$@ZnCoO-NS electrode (0.012 V) at current density of 3 mA cm^{-2}, illustrating that the ZnCoS scaffold can effectively reduce the overall resistance. Moreover, there is no significant change in the IR of the $Ni(OH)_2$@ZnCoS-NS electrode as the current density increases (Fig. 4e), convincingly revealing improved capacitive behavior. EIS results are well coincident with the above analysis as shown in Fig. 4f. For $Ni(OH)_2$@ZnCoS-NSs, the values of R_{ESR} (0.2 Ω) and R_{ct} (0.43 Ω) are smaller than those for $Ni(OH)_2$@ZnCoO-NSs (0.63 Ω and 1.71 Ω), demonstrating a much enhanced conductivity in both the serial and charge transfer parts. Apart from the superior conductivity of ZnCoS, we find that enhanced structural flexibility occurs in the bimetallic sulfide crystal structure especially when compared with bimetallic oxides (ZnCoO) and monometal sulfides (CoS), thus creating a more stable heterostructure to accommodate mechanical deformation in the electrochemical process. To investigate the elastic properties of the crystal structures of ZnCoS, ZnCoO, and CoS, the formula of elastic moduli and mechanical stability criteria are introduced for the considered crystal systems (cubic ZnCoO and hexagonal ZnCoS/CoS) and the corresponding computational details are given in the calculation sections and Table S2 (ESI†).[47–49] Voigt–Reuss–Hill approximations have been widely adopted to calculate mechanical parameters of cubic and hexagonal crystal systems,[50] such as bulk modulus (B) and shear modulus (G). Thus, Young's modulus Y can be calculated using the following formula: $Y = 9BG/(3B + G)$.

Table 1 Young's modulus Y (Gpa), bulk modulus B (Gpa), and shear modulus G (Gpa) for cubic ZnCoO and hexagonal CoS and ZnCoS

Sample	Y	B	G	B/G
ZnCoO	4691.28	4011.10	1797.33	2.23
CoS	2534.18	2262.34	964.81	2.34
ZnCoS	2287.54	2200.31	862.10	2.55

The calculated mechanical parameters are listed in Table 1. As can be seen from the metallic oxide (ZnCoO) to metallic sulfides (ZnCoS or CoS), the Y, B and G values for both ZnCoS and CoS decrease by nearly half, which is mainly attributed to the lower electronegativity and larger atomic radius leading to a softer structural property compared with that of ZnCoO. Moreover, the Zn doping increases the Co–S bond length from 2.32 Å to 2.50 Å (Fig. 4d) and further enhances the elastic property of ZnCoS. The B/G of 2.55 for ZnCoS is the smallest among the considered crystal structures, indicating that ZnCoS possesses a more ductile structure which is prone to strain

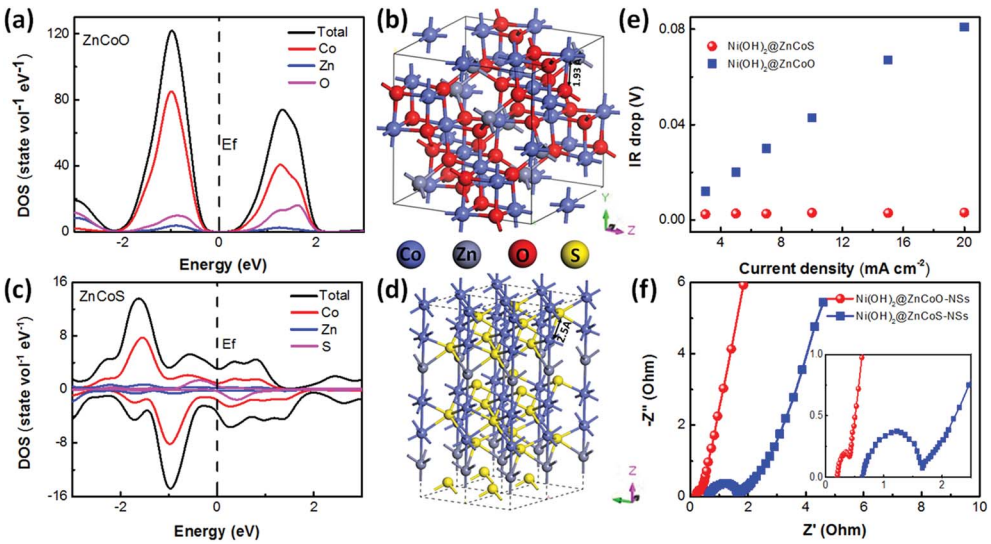

Fig. 4 The density of states (DOS) for (a) ZnCoO and (c) ZnCoS and the optimized crystal structures of (b) ZnCoO and (d) ZnCoS; E_f represents the Fermi level; (e) the IR drop of $Ni(OH)_2$@ZnCoS-NS and $Ni(OH)_2$@ZnCoO-NS electrodes recorded over different current densities from 3 to 20 mA cm^{-2} and (f) comparison of Nyquist plots of $Ni(OH)_2$@ZnCoS-NS and $Ni(OH)_2$@ZnCoO-NS electrodes.

relaxation and serves as a buffering phase for the volume changes of the active materials during the redox process, effectively preventing the collapse of the heterostructures. Compared with $Ni(OH)_2$@ZnCoS-NSs (Fig. S5, ESI†), SEM images reveal that the $Ni(OH)_2$@ZnCoO nanosheets seriously deform and collapse after 10 000 cycling tests (Fig. S7, ESI†) primarily because the brittle ZnCoO structure as the scaffold cannot accommodate the volume changes occurring during the redox process. With all of these advantages, in terms of the scaffold for constructing core–shell heterostructures, Zn/Co-MOF-derived ZnCoS nanosheets can be an ideal secondary substrate for the growth of other active materials with exceptional electrochemical performances for ASC systems.

Recently, VN has been considered the most promising candidate for high-performance negative electrode materials because of its higher specific capacitance and energy density as a result of its reversible and rapid redox reactions. For the purpose of assembling the FSASCs with high capacitance and energy density, VN@ZnCoS-NSs have been synthesized as the negative electrode, and their morphology and microstructure are studied by SEM and TEM techniques. Similar to the $Ni(OH)_2$@ZnCoS-NSs, the pristine ZnCoS-NSs array is evenly covered with a VN coating (Fig. 5a). Such a vertically geometric framework allows the effective permeation of electrolytes and prevents the agglomeration of the VN active material during the hydrothermal process. As shown in Fig. 5b and c, VN@ZnCoS-NSs possess a rough surface which consists of numerous randomly distributed tiny particles on the exposed surface, which can provide abundant electroactive sites and offer sufficient contact with the electrolyte leading to extraordinary faradaic redox activities. The high-resolution TEM (Fig. 5d) image is obtained from a section of the as-synthesized VN@ZnCoS-NSs, and shows that the interplanar spacing is about 0.236 nm which corresponds to the (111) plane of monoclinic VN.[8] To confirm the compositional distribution of nanosheets, the elemental mapping results evidently show that the Co, Zn, S, V, and N elements coexist and are homogeneously distributed throughout the nanosheet morphology (Fig. 5e).

To estimate the electrochemical performance, CV, GCD, and EIS of the as-made electrodes are investigated employing a three-electrode measuring system in a 2 M KOH aqueous electrolyte. The typical comparison of the CV curves of the VN@ZnCoS-NSs and unitary VN nanosheets directly grown on the CC substrate (Fig. S8a and b, ESI†) at a scan rate of 50 mV s^{-1} is shown in Fig. 5f. As expected, the integral area of the VN@ZnCoS-NS electrode is obviously larger than that of the unitary VN nanosheet electrode, indicating that the heterostructure electrode possesses a much higher capacitance. This difference is ascribed to the increased electrical conductivity of the ZnCoS scaffolds and the structural merits of upright arrays. Furthermore, both the core and shell of the VN@ZnCoS-NSs are good pseudocapacitive materials that undergo redox reactions with ions in the electrolyte, hence enhancing the whole capacitance. From the plots of peak current (i) *versus* square root of scan rate ($v^{1/2}$) from 10 to 100 mV s^{-1},[51,52] the b-value for the VN@ZnCoS-NS electrode (0.84) is greater than that for the VN nanosheet electrode (0.67), indicating the better, and thus faster, kinetics of the VN@ZnCoS-NS electrode. As shown in Fig. 5h, two broad redox humps during the anodic (−0.7 to −0.6 V) and cathodic (−0.8 to −0.9 V) scans are observed, indicating that the capacitive property of the VN@ZnCoS-NS electrode is composed of pseudocapacitance and electrical double capacitance. Importantly, the CV curve retains a similar shape without deformation even as the scan rate increases to an ultrahigh value of 100 mV s^{-1}, indicating the excellent rate capability. The high specific capacitance and rate capability of the electrode are also revealed by GCD measurements (Fig. 5i). The impedance spectra of both electrodes exhibit similar semicircles in the high frequency region and straight lines in the low frequency region. Clearly, the VN@ZnCoS-NS electrode has a smaller R_{ct} (1.3 Ω) than the VN nanosheet electrode (2.4 Ω), which demonstrates that the heterostructure electrode possesses enhanced charge transfer kinetics. Fig. 5k displays the comparison of the specific capacitance of the VN@ZnCoS-NS and unitary VN nanosheet electrodes. Obviously, the capacitance of the VN@ZnCoS-NSs is always higher than that of the unitary VN nanosheets at all current densities. The VN@ZnCoS-NS electrode exhibits a high capacitance of 1.35 F cm^{-2} at a current density of 3 mA cm^{-2}, which is about 2 times higher than that of the VN nanosheet electrode. Even at a high current density of 20 mA cm^{-2}, the capacitance can still reach 0.78 F cm^{-2} (about 60% capacitance retention compared to that at 3 mA cm^{-2}). In general, VN electrode materials often suffer from poor electrochemical stability because the morphology of VN commonly consisting of weakly interconnected nanoparticles is unavoidably deformed or even destroyed during cycling. To evaluate the long-term sustainability, their cycling stability is tested at a current density of 10 mA cm^{-2}, as shown in Fig. 5l. Interestingly, the core–shell heterostructure exhibits a much higher stability than the unitary VN nanosheets. After 10 000 consecutive cycles, the VN@ZnCoS-NSs still retain 80% of their initial capacitance, while the capacitance of the unitary VN nanosheets decreases continuously and only about 40% of the initial capacitance is retained. In addition, the morphologies of the two electrodes before and after cycling are also given in Fig. S8 (ESI†). It can be clearly seen that there is no obvious change in the heterostructure nanosheet morphology after testing for 10 000 cycles (Fig. S8d†), which mainly benefits from the stable heterostructure being able to accommodate volume changes during the cycling process. In contrast, the unitary VN nanosheets covered on the CC substrate seriously collapse caused by detachment after the cycling test (Fig. S8c†). Thus, with this ZnCoS nanosheet scaffold, we are able to construct VN negative electrode materials with superior electrochemical performance which is necessary for ASC devices.

To further evaluate the practical applications of the as-fabricated electrode materials, a highly efficient ASC device is constructed using the $Ni(OH)_2$@ZnCoS-NSs and VN@ZnCoS-NSs as the positive electrode and negative electrode, respectively. Fig. S10a (ESI†) displays the CV curves of the as-fabricated electrodes in separate potential windows at a scan rate of 10 mV s^{-1}. Taking advantage of the complementary potential windows and matching capacitance, it is expected that the working voltage of the ASC device can be extended up to 1.6 V. A

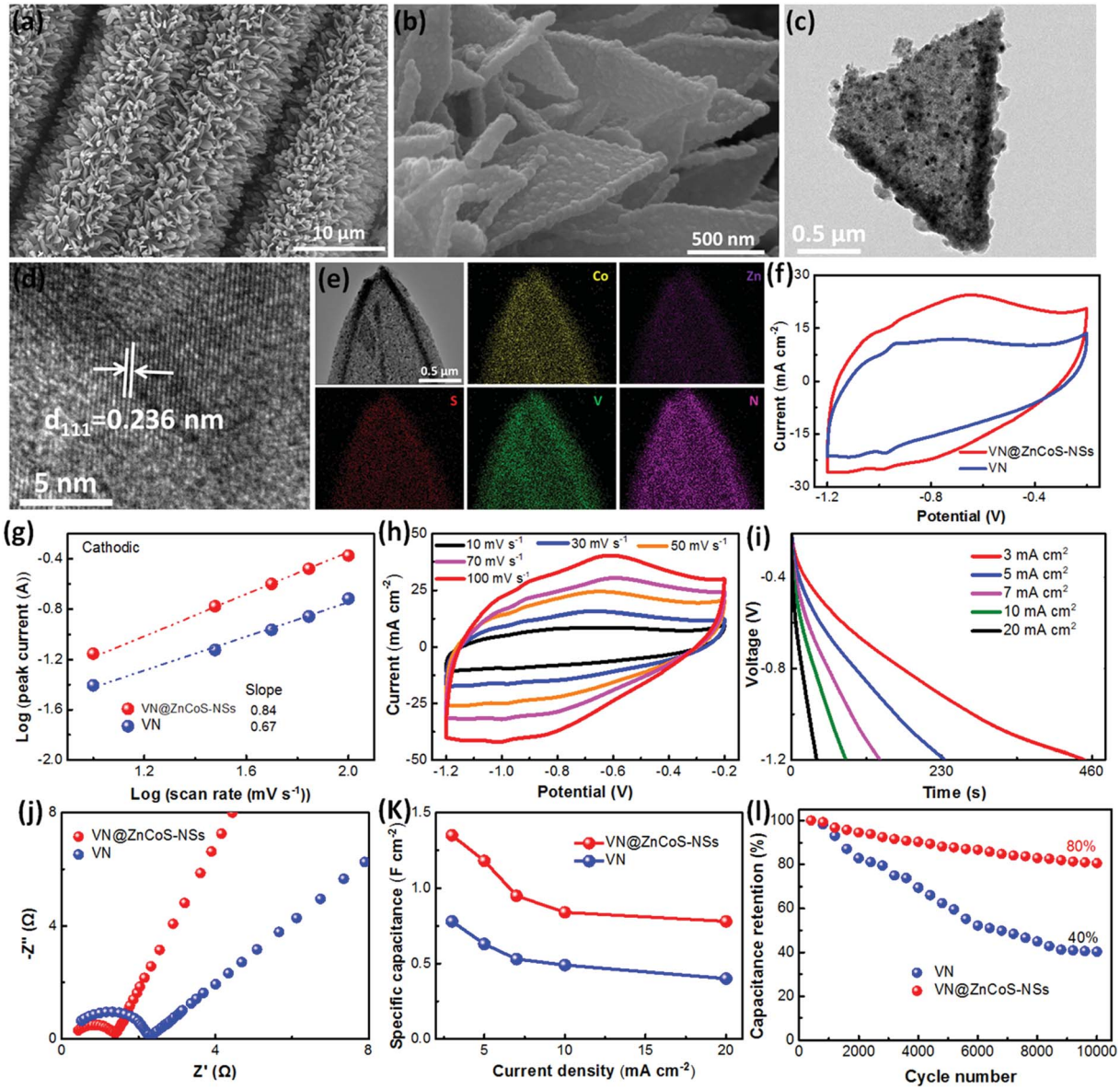

Fig. 5 Low (a) and high (b) magnification SEM images of VN@ZnCoS-NSs; (c) typical TEM image, (d) HRTEM image and (e) EDS mapping results of VN@ZnCoS-NSs. Comparison of electrochemical performance of VN@ZnCoS-NSs and unitary VN electrodes in a three-electrode system with a 2 M KOH solution: (f) CV curves measured at a scan rate of 50 mV s^{-1}, (g) *b*-value determination of the cathodic peak currents from 10 to 100 mV s^{-1}, (h) CV curves at various scan rates and (i) GCD profiles at different current densities for VN@ZnCoS-NSs, (j) comparison of Nyquist plots, (k) specific capacitance values *versus* current density, and (l) cycling performance at a high current density of 100 mA cm^{-2}.

sequence of CV tests at a scan rate of 30 mV s^{-1} with various potential windows ranging from 0.6 to 1.6 V are conducted to evaluate the operating potential of the ASC as shown in Fig. 6a. The CV curves retain similar rectangular shapes without obvious redox peaks even when the cell voltage increases to 1.6 V, indicating the excellent kinetics of electrochemical reactions and good capacitive behavior of the ASC electrode. The corresponding GCD curves of the ASC device at a current density of 7 mA cm^{-2} with different voltage windows are shown in Fig. S10b (ESI†). The GCD curves show a nearly symmetric triangular shape without distortion as the operating potential is increased to 1.6 V, which demonstrates that the device possesses good reversibility and low equivalent series resistance. The EIS spectrum of the ASC shows a small semicircle in the high-frequency area (Fig. S10c, ESI†), suggesting a rapid charge transfer process of the device at the electrolyte–electrode interface. In addition, from the plot, it can be clearly see that it also presents low diffusion resistance, which implies that the device possesses good electrical conductivity. The areal specific capacitances and energy density of the ASC device are also calculated from the GCD curves collected at 7 mA cm^{-2} as a function of the potential window (Fig. S10d, ESI†). Notably, with the potential window extended from 0.6 to 1.6 V, the areal specific capacitance significantly increases from 198 to 433 mF cm^{-2} and the energy density similarly improves from 9.9 to 154 μW h cm^{-2}. To further investigate the capacitive behavior of the

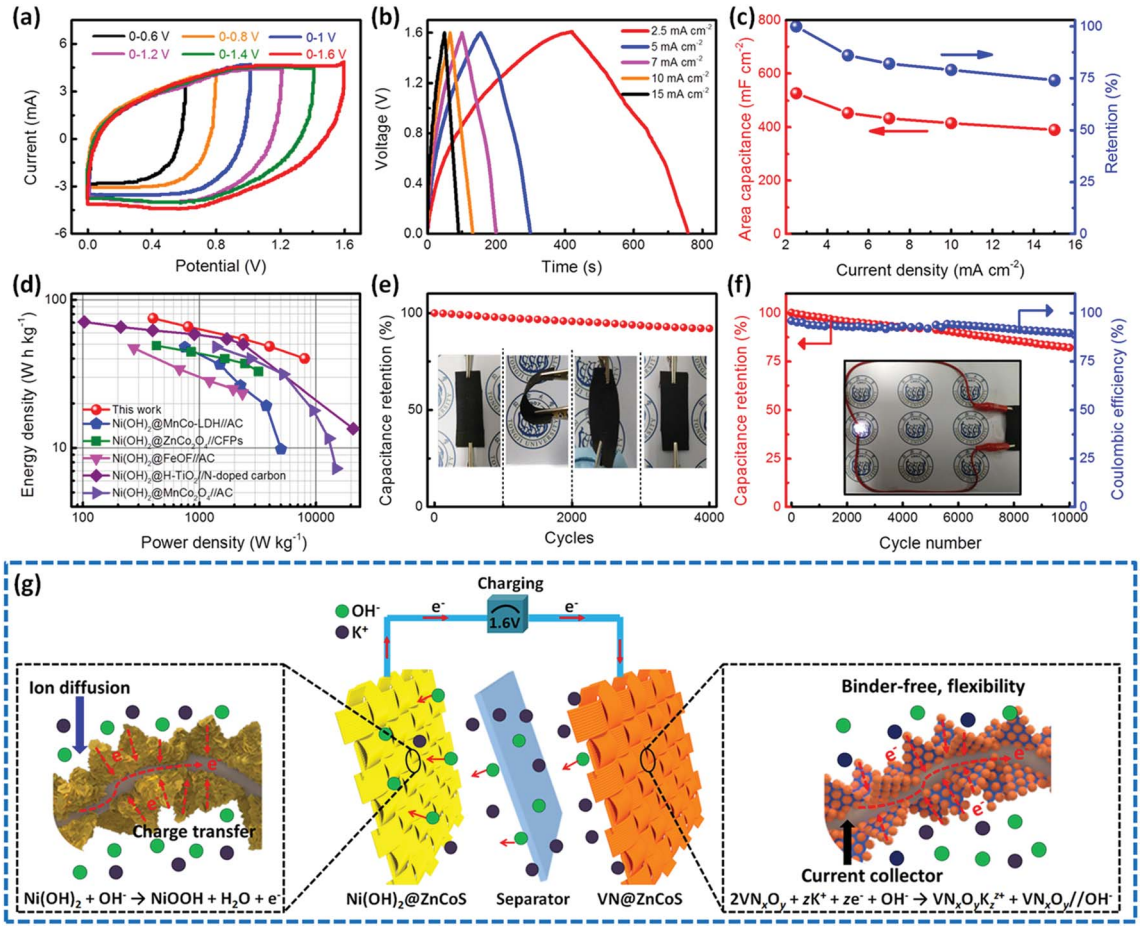

Fig. 6 (a) CV curves of the $Ni(OH)_2$@ZnCoS-NS//VN@ZnCoS-NS ASC device in different voltage windows at a scan rate of 30 mV s^{-1}, (b) GCD curves of the $Ni(OH)_2$@ZnCoS-NS//VN@ZnCoS-NS ASC device between 0 and 1.6 V at different current densities, (c) the specific capacitance and corresponding capacitance retention of the ASC device as a function of current density, (d) the Ragone plots of the $Ni(OH)_2$@ZnCoS-NS//VN@ZnCoS-NS ASC and reported ASCs in literature, (e) the capacitance retention of the ASC device at flat, bent, and twisted states during the test over 4000 cycles, (f) the cycling stability and corresponding coulombic efficiency of the ASC device (the inset in (f) presents the digital image of the $Ni(OH)_2$@ZnCoS-NS//VN@ZnCoS-NS ASC lighting an LED), and (g) electrode design and charge storage mechanism of $Ni(OH)_2$@ZnCoS-NS positive electrode and VN@ZnCoS-NS negative electrode in the present ASC device.

asymmetric device, galvanostatic charge/discharge measurements between 0 and 1.6 V are also carried out at various current densities from 2.5 to 15 mA cm^{-2}. The nearly symmetrical GCD curves at all current densities in Fig. 6b indicate the high coulombic efficiency and reversible faradaic reactions. And the linear charge/discharge features in the GCD profiles are expressly observed, which again confirms the ideal capacitive properties. As presented in Fig. 6c, the areal specific capacitance of our ASC device is calculated based on the GCD curves and plotted as a function of current density. It is worth noting that the areal specific capacitance of the device at 2.5 mA cm^{-2} is as high as 527 mF cm^{-2}; when the current density is increased up to 15 mA cm^{-2}, the device still delivers a high capacitance of 390 mF cm^{-2}, around 74% retention of its initial value, suggesting a prominent rate performance for the ASC device. Significantly, based on the total mass of the active materials, the $Ni(OH)_2$@ZnCoS-NS//VN@ZnCoS-NS ASC can deliver intriguing mass specific capacitances of 210.7, 185.3, 150.1, 136.5, and 113.3 F g^{-1} at current densities of 0.5, 1, 3, 5, and 10 A g^{-1}, respectively, as shown in Fig. S11 (ESI†). Energy density and power density are two critical parameters for evaluating the practical applications of energy storage devices. Fig. 6d compares the energy and power densities of the constructed ASC device reported in this work to the values reported for other ASCs. In this work, the $Ni(OH)_2$@ZnCoS-NS//VN@ZnCoS-NS ASC device with a cell voltage of 1.6 V exhibits a peak energy density of 75 W h kg^{-1} at a power density of 0.4 kW kg^{-1}, and can still retain 40.1 W h kg^{-1} at a power density of 8 kW kg^{-1}. Impressively, the specific energy density reported here is substantially higher than that reported for $Ni(OH)_2$-based heterostructures for ASCs, such as $Ni(OH)_2$@MnCo-LDH//AC (47.9 W h kg^{-1}),[53] $Ni(OH)_2$@$ZnCo_2O_4$//CFPs (49 W h kg^{-1}),[54] $Ni(OH)_2$@FeOF//AC (47.1 W h kg^{-1}),[43] $Ni(OH)_2$@H-TiO_2//N–C (70.9 W h kg^{-1}),[41] and $Ni(OH)_2$@$MnCo_2O_4$//AC (48 W h kg^{-1}).[13] Besides the ultrahigh mass energy density, the present $Ni(OH)_2$@ZnCoS-NS//VN@ZnCoS-NS ASC can also deliver a remarkable volumetric energy density of about 3.13 mW h cm^{-3} and a volumetric power density of 53.5 mW cm^{-3} obtained at a current density of 2.5 mA cm^{-2},

which tremendously exceeds previously published data of quasi/all-solid-state supercapacitors (Table S3, ESI†). Even at a high power density of 320 mW cm^{-3}, the ASC can still achieve an energy density of about 2.31 mW h cm^{-3}, demonstrating superior power capability. To demonstrate the mechanical flexibility of the constructed ASC device, the capacitance retention of the ASC device at different bending/twisting cycles is shown in Fig. 6e. 92% of the initial capacitance can be well preserved after 4000 cycles at 10 mA cm^{-2} even when the device is continuously bent/twisted during the test (inset in Fig. 6e), revealing good flexibility and potential application in flexible electronics. Apart from the excellent mechanical flexibility, the $Ni(OH)_2$@ZnCoS-NS//VN@ZnCoS-NS ASC also exhibits outstanding cycling stability in the long-term cycling test. Fig. 6f shows the capacitance retention of the device as a function of cycle number for 10 000 charge/discharge cycles at a current density of 10 mA cm^{-2}. Most noticeably, only 8% capacitance attenuation is observed after the device is charged/discharged over 5000 cycles, and it still retains around 82% of its original capacitance even after 10 000 cycles, indicating an excellent cycling stability which is highly promising for practical applications. This is primarily attributed to the structural stability and flexibility of the ZnCoS nanosheet scaffold with array structures, which not only leads to the homogeneous dispersion of the $Ni(OH)_2$ and VN and relaxes the strain of active materials in the electrochemical process, avoiding their structural collapse, but also allows for efficient charge transport between the active materials and the conductive scaffold. Moreover, Fig. 6f shows that the device can exhibit high coulombic efficiencies (>90%, blue curve) over 10 000 cycles, illustrating high charge transfer efficiencies over long-term cycling. To show the practical applications of the $Ni(OH)_2$@ZnCoS-NS//VN@ZnCoS-NS ASC, the constructed device is connected to a white light emitting diode (LED) and successfully lit it (inset in Fig. 6f). The schematic representation and operating principles of the as-assembled ASC device based on the $Ni(OH)_2$@ZnCoS-NS positive and VN@ZnCoS-NS negative electrode materials are expounded in Fig. 6g. When the ASC is charged, the $Ni(OH)_2$@ZnCoS-NS positive electrode undergoes an oxidization reaction following the process of $Ni(OH)_2 + OH^- \rightarrow NiOOH + H_2O + e^-$,[55,56] and the VN@ZnCoS-NS negative electrode is reduced, described as $2VN_xO_y + zK^+ + ze^- + OH^- \rightarrow VN_xO_yK_z^{z+} + VN_xO_y//OH^-$,[57,58] which occurs fast at the surface of the active materials leading to super high pseudocapacitance. The extraordinary capacitive performance of our ASC device is primarily attributed to the rational design and construction of 3D well-aligned core–shell heterostructures on the carbon cloth by using bimetallic MOF-derived ZnCoS nanosheets as a secondary substrate. Specifically, we highlight the following features: (1) 2D Zn/Co-MOF-derived ZnCoS nanosheet arrays are directly grown on the carbon cloth, which greatly ensures that the ZnCoS nanosheet arrays stick tightly to the carbon cloth (the current collector as shown in Fig. 6g) to form strong adhesion and build up an expressway for charge transfer, thus obtaining integrated and binder-free electrodes with flexibility. (2) The scaffold, ZnCoS-NSs with a ductile crystal structure, can play the role of a mechanical buffer that undertakes the volume change of the active materials during the electrochemical reactions and effectively prevents the core–shell heterostructure from deformation and fragmentation. Moreover, these 2D nanosheet arrays are capable of interconnecting with each other by growing active materials on it to construct 3D networks with abundant exposed surfaces, which can not only provide express channels for facile diffusion of the electrolyte ions but also improve the utilization efficiency of the active materials. (3) The homogeneously distributed $Ni(OH)_2$ nanoflakes and VN nanoparticle coating as the shell are directly grown on the surfaces of the ZnCoS nanosheet arrays by scalable synthesis and provide free open active sites for accessible contact with the electrolyte, thus providing a short ion diffusion path during the charge/discharge process. (4) As for the ASC structure, the pseudocapacitive VN negative electrode material not only overcomes the small capacity of the traditional double layer carbon negative electrode, but also matches the supercapacitance and cell voltage windows of the positive electrode materials in order to achieve the maximum energy density of the ASC device. Consequently, the cooperative contribution from the ZnCoS nanosheets as well as $Ni(OH)_2$ nanoflakes and VN nanoparticle coating together with the advantages of the core–shell heterostructures enables the device to exhibit exceptional electrochemical performance.

4. Conclusions

In summary, we demonstrate an effective MOF-derived approach to construct high-performance positive and negative electrode materials with a core–shell heterostructure for ASCs that deliver both high energy and power densities (energy density of 75 W h kg^{-1} at a power density of 0.4 kW kg^{-1}). The large-area ZnCoS nanosheet arrays directly grown on CC are successfully fabricated using Zn/Co-MOF arrays as the reactive template. The as-made ZnCoS nanosheet arrays with excellent conductivity and ductile structure offer an electrically and ionically conducting 3D continuous network for the growth of active materials. Based on this platform, the originally built $Ni(OH)_2$@ZnCoS-NSs are validated to be a highly capacitive positive electrode (8.1 F cm^{-2} at 3 mA cm^{-2}, *i.e.*, 2730 F g^{-1}), matching well with the similarly constructed VN@ZnCoS-NS negative electrode (1.35 F cm^{-2} at 3 mA cm^{-2}). Due to the rationally engineered electrodes, the ASC device achieves excellent specific capacitance (210.7 F g^{-1} at 0.5 A g^{-1}), stable electrochemical stability (82% capacitance retention even after 10 000 cycles), and good structural flexibility. This study not only offers a useful and available strategy for the design of high-performance heterostructure electrodes for ASCs by exploiting the compositional and structural versatility of 2D MOF arrays, but also opens a new avenue for applications in high-performance electrochemical energy storage.

Conflicts of interest

The authors declare no competing financial interest.

Acknowledgements

The authors acknowledge the support of the National Natural Science Foundation of China [grant No. U1503292 and grant No. 51872204] and the National Key Research and Development Program of China [grant No. 2017YFA0204600].

Notes and references

1 J. A. Roger, T. Someya and Y. Huang, *Science*, 2010, **327**, 1603–1607.
2 B. Guan, L. Yu, X. Wang, S. Song and X. W. Lou, *Adv. Mater.*, 2017, **29**, 1605051.
3 D. Xu, D. Chao, H. Wang, Y. Gong, R. Wang, B. He, X. Hu and H. Fan, *Adv. Energy Mater.*, 2018, **8**, 1702769.
4 J. R. Miller and P. Simon, *Science*, 2008, **321**, 651–652.
5 N. Choudhary, C. Li, J. Moore, N. Nagaiah, L. Zhai, Y. Jung and J. Thomas, *Adv. Mater.*, 2017, **29**, 1605336.
6 P. Y. Tang, L. J. Han, A. Genç, Y. M. He, X. Zhang, L. Zhang, J. R. G. Mascarós, J. R. Morante and J. Arbiol, *Nano Energy*, 2016, **22**, 189–201.
7 J. Yang, C. Yu, X. M. Fan, S. X. Liang, S. F. Li, H. W. Huang, Z. Ling, C. Hao and J. S. Qiu, *Energy Environ. Sci.*, 2016, **9**, 1299–1307.
8 Q. C. Zhang, X. N. Wang, Z. H. Pan, J. Sun, J. X. Zhao, J. Zhang, C. X. Zhang, L. Tang, J. Luo, B. Song, Z. X. Zhang, W. B. Lu, Q. W. Li, Y. G. Zhang and Y. G. Yao, *Nano Lett.*, 2017, **17**, 2719–2726.
9 J. Jiang, Y. Y. Li, J. P. Liu, X. T. Huang, C. Z. Yuan and X. W. Lou, *Adv. Mater.*, 2012, **24**, 5166.
10 S. Sun, T. Zhai, C. L. Liang, S. V. Savilov and H. Xia, *Nano Energy*, 2018, **45**, 390–397.
11 J. Yan, Z. J. Fan, W. Sun, G. Q. Ning, T. Wei, Q. Zhang, R. F. Zhang, L. J. Zhi and F. Wei, *Adv. Funct. Mater.*, 2012, **22**, 2632.
12 M. Guo, J. Wang, H. Dou, G. Gao, S. Wang, J. Wang, Z. Xiao, G. Wu, X. Yang and Z. F. Ma, *Nano Energy*, 2019, **56**, 502–511.
13 X. Xia, J. Tu, Y. Zhang, J. Chen, X. Wang, C. Gu, C. Guan, J. Luo and H. J. Fan, *Chem. Mater.*, 2012, **24**, 3794–3799.
14 L. Huang, D. Chen, Y. Ding, S. Feng, Z. Wang and M. Liu, *Nano Lett.*, 2013, **13**, 3135–3139.
15 Y. Zhao, L. Hu, S. Zhao and L. Wu, *Adv. Funct. Mater.*, 2016, **26**, 4085.
16 Y. B. Zhang, B. Wang, F. Liu, J. P. Cheng, X. W. Zhang and L. Zhang, *Nano Energy*, 2016, **27**, 627–637.
17 Q. C. Zhang, W. W. Xu, J. Sun, Z. H. Pan, J. X. Zhao, X. N. Wang, J. Zhang, P. Man, J. B. Guo, Z. Y. Zhou, B. He, Z. X. Zhang, Q. W. Li, Y. G. Zhang, L. Xu and Y. G. Yao, *Nano Lett.*, 2017, **17**, 7552–7560.
18 C. Y. Cui, J. T. Xu, L. Wang, D. Guo, M. L. Mao, J. M. Ma and T. H. Wang, *ACS Appl. Mater. Interfaces*, 2016, **8**, 8568–8575.
19 W. D. He, C. G. Wang, H. Q. Li, X. L. Deng, X. J. Xu and T. Y. Zhai, *Adv. Energy Mater.*, 2017, **7**, 1700983.
20 J. Zhou, L. Wang, M. Yang, J. Wu, F. Chen, W. Huang, N. Han, H. Ye, F. Zhao, Y. Li and Y. Li, *Adv. Mater.*, 2017, **29**, 1702061.
21 P. Zhang, B. Y. Guan, L. Yu and X. W. Lou, *Angew. Chem., Int. Ed.*, 2017, **56**, 7141–7145.
22 Y. Li, J. Xu, T. Feng, Q. F. Yao, J. P. Xie and H. Xia, *Adv. Funct. Mater.*, 2017, **27**, 1606728.
23 B. Y. Guan, X. Y. Yu, H. B. Wu and X. W. Lou, *Adv. Mater.*, 2017, **29**, 1703614.
24 F. Yu, X. Xiong, L. Y. Zhou, J. L. Li, J. Y. Liang, S. Q. Hu, W. T. Lu, B. Li and H. C. Zhou, *J. Mater. Chem. A*, 2019, **7**, 2875–2883.
25 M. S. Javed, N. Shaheen, S. Hussain, J. Li, S. S. A. Shah, Y. Abbas, M. A. Ahmad, R. Raza and W. Mai, *J. Mater. Chem. A*, 2019, **7**, 946–957.
26 C. Qu, Z. Liang, Y. Jiao, B. Zhao, B. Zhu, D. Dang, S. Dai, Y. Chen, R. Zou and M. Liu, *Small*, 2018, **14**, 1800285.
27 D. M. Xu, D. L. Chao, H. W. Wang, Y. S. Gong, R. Wang, B. B. He, X. L. Hu and H. J. Fan, *Adv. Energy Mater.*, 2018, **8**, 1702769.
28 C. Guan, X. M. Liu, W. N. Ren, X. Li, C. W. Cheng and J. Wang, *Adv. Energy Mater.*, 2017, **7**, 1602391.
29 X. H. Xia, C. R. Zhu, J. S. Luo, Z. Y. Zeng, C. Guan, C. F. Ng, H. Zhang and H. J. Fan, *Small*, 2014, **10**, 766–773.
30 Y. Huang, L. Quan, T. Liu, Q. Chen, D. Cai and H. Zhan, *Nanoscale*, 2018, **10**, 14171–14181.
31 W. N. Ren, H. F. Zhang, C. Guan and C. W. Cheng, *Adv. Funct. Mater.*, 2017, **27**, 1702116.
32 C. Z. Yuan, J. Y. Li, L. Hou, X. G. Zhang, L. F. Shen and X. W. Lou, *Adv. Funct. Mater.*, 2012, **22**, 4592.
33 J. Yang, F. J. Zhang, H. Y. Lu, X. Hong, H. L. Jiang, Y. Wu and Y. D. Li, *Angew. Chem.*, 2015, **127**, 11039–11043.
34 Z. Q. Liu, H. Cheng, N. Li, T. Y. Ma and Y. Z. Su, *Adv. Mater.*, 2016, **28**, 3777.
35 S. J. Hao, B. W. Zhang, S. Ball, M. Copley, Z. C. Xu, M. Srinivasan, K. Zhou, S. Mhaisalkar and Y. Z. Huang, *J. Power Sources*, 2015, **294**, 112–119.
36 J. Zhu, S. Tang, J. Wu, X. Shi, B. Zhu and X. Meng, *Adv. Energy Mater.*, 2016, **160**, 1234.
37 M. K. Aslam, S. S. A. Shah, S. Li and C. Chen, *J. Mater. Chem. A*, 2018, **6**, 14083–14090.
38 W. W. Liu, C. X. Lu, K. Liang and B. K. Tay, *J. Mater. Chem. A*, 2014, **2**, 5100–5107.
39 C. Z. Yuan, H. B. Wu, Y. Xie and X. W. Lou, *Angew. Chem., Int. Ed.*, 2014, **53**, 1488–1504.
40 Y. Zhao, X. F. Li, B. Yan, D. B. Xiong, D. J. Li, S. Lawes and X. L. Sun, *Adv. Energy Mater.*, 2016, **6**, 1502175.
41 Q. Q. Ke, C. Guan, X. Zhang, M. Zheng, Y. W. Zhang, Y. Q. Cai, H. Zhang and J. Wang, *Adv. Mater.*, 2017, **29**, 1604164.
42 B. Dong, M. Li, S. Chen, D. Ding, W. Wei, G. Gao and S. Ding, *ACS Appl. Mater. Interfaces*, 2017, **9**, 17890–17896.
43 M. Q. Wang, Z. Q. Li, C. X. Wang, R. Z. Zhao, C. X. Li, D. X. Guo, L. Y. Zhang and L. W. Yin, *Adv. Funct. Mater.*, 2017, **27**, 1701014.
44 J. Zhao, Z. J. Li, X. C. Yuan, Z. Yang, M. Zhang, A. Meng and Q. D. Li, *Adv. Energy Mater.*, 2018, **8**, 1702787.
45 S. Kumar, G. Saeed, N. H. Kim and J. H. Lee, *J. Mater. Chem. A*, 2018, **6**, 7182–7193.

46 Z. Tang, C. Tang and H. Gong, *Adv. Funct. Mater.*, 2012, **22**, 1272.
47 J. Haines, J. M. Leger and G. Bocquillon, *Annu. Rev. Mater. Res.*, 2001, **31**, 1.
48 J. P. Watt and L. Peselnick, *J. Appl. Phys.*, 1980, **51**, 1525.
49 J. F. Nye, *Physical Properties of Crystals*, Oxford University Press, Oxford, 1985.
50 R. Hill, *Proc. Phys. Soc., London, Sect. A*, 1952, **65**, 349.
51 V. Augustyn, J. Come, M. A. Lowe, J. W. Kim, P.-L. Taberna, S. H. Tolbert, H. D. Abruna, P. Simon and B. Dunn, *Nat. Mater.*, 2013, **12**, 518–522.
52 P. L. Lou, Z. G. Cui, Z. Q. Jia, J. Y. Sun, Y. B. Tan and X. G. Guo, *ACS Nano*, 2017, **11**, 3705–3715.
53 S. Liu, S. C. Lee, U. Patil, I. Shackery, S. Kang, K. Zhang, J. H. Park, K. Y. Chung and S. C. Jun, *J. Mater. Chem. A*, 2017, **5**, 1043–1049.
54 Y. Pan, H. Gao, M. Y. Zhang, L. Li, G. G. Wang and X. Y. Shan, *J. Colloid Interface Sci.*, 2017, **497**, 50–56.
55 M. J. Xie, Z. C. Xu, S. Y. Duan, Z. F. Tian, Y. Zhang, K. Xiang, M. Lin, X. F. Guo and W. P. Ding, *Nano Res.*, 2018, **11**, 216.
56 X. H. Xiong, D. Ding, D. C. Chen, G. Waller, Y. F. Bu, Z. X. Wang and M. Liu, *Nano Energy*, 2015, **11**, 154–161.
57 D. Choi, G. E. Blomgren and P. N. Kumta, *Adv. Mater.*, 2006, **18**, 1178.
58 X. H. Lu, M. H. Yu, T. Zhai, G. M. Wang, S. L. Xie, T. Y. Liu, C. L. Liang, Y. X. Tong and Y. Li, *Nano Lett.*, 2013, **13**, 2628–2633.